ACS APPLIED NANO MATERIALS

Open Access

This article is licensed under CC-BY 4.0

www.acsanm.org

Article

Nanomechanical Modeling of the Bending Response of Silicon Nanowires

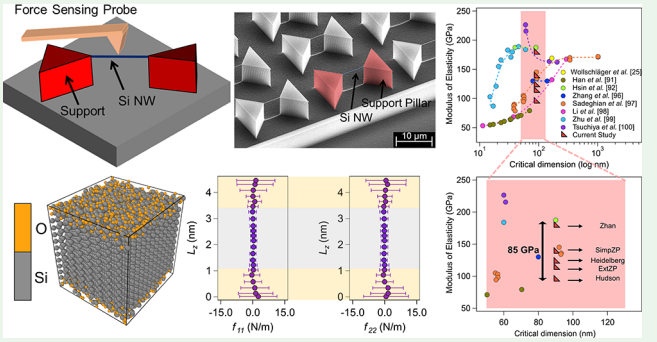
Sina Zare Pakzad, Mohammad Nasr Esfahani, Zuhal Tasdemir, Nicole Wollschläger, Taotao Li, XueFei Li, Mustafa Yilmaz, Yusuf Leblebici, and B. Erdem Alaca*

Cite This: *ACS Appl. Nano Mater.* 2023, 6, 15465−15478

Read Online

ACCESS | Metrics & More | Article Recommendations | Supporting Information

ABSTRACT: Understanding the mechanical behavior of silicon nanowires is essential for the implementation of advanced nanoscale devices. Although bending tests are predominantly used for this purpose, their findings should be properly interpreted through modeling. Various modeling approaches tend to ignore parts of the effective parameter set involved in the rather complex bending response. This oversimplification is the main reason behind the spread of the modulus of elasticity and strength data in the literature. Addressing this challenge, a surface-based nanomechanical model is introduced in this study. The proposed model considers two important factors that have so far remained neglected despite their significance: (i) intrinsic stresses composed of the initial residual stress and surface-induced residual stress and (ii) anisotropic implementation of surface stress and elasticity. The modeling study is consolidated with molecular dynamics-based study of the native oxide surface through reactive force fields and a series of nanoscale characterization work through *in situ* three-point bending test and Raman spectroscopy. The treatment of the test data through a series of models with increasing complexity demonstrates a spread of 85 GPa for the modulus of elasticity and points to the origins of ambiguity regarding silicon nanowire properties, which are some of the most commonly employed nanoscale building blocks. A similar conclusion is reached for strength with variations of up to 3 GPa estimated by the aforementioned nanomechanical models. Precise consideration of the nanowire surface state is thus critical to comprehending the mechanical behavior of silicon nanowires accurately. Overall, this study highlights the need for a multiscale theoretical framework to fully understand the size-dependent mechanical behavior of silicon nanowires, with fortifying effects on the design and reliability assessment of future nanoelectromechanical systems.



KEYWORDS: *silicon nanowires, native oxide, surface stress, surface elasticity, mechanical behavior, bending test, Raman spectroscopy, molecular dynamics*

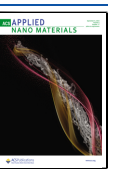
Downloaded via KOC UNIV on March 23, 2024 at 12:12:35 (UTC).
See https://pubs.acs.org/sharingguidelines for options on how to legitimately share published articles.

INTRODUCTION

Silicon (Si) nanowires (NWs) are essential building blocks in nanoelectromechanical systems (NEMS) and nanoelectronics.[1,2] Because of their compatibility with semiconductor manufacturing, Si NWs bear potential for improving existing technologies or generating new approaches regarding mass spectroscopy,[3,4] electromechanical/biochemical sensors,[5,6] field effect transistors (FETs),[7−9] energy conversion, and harvesting and storage media.[10] The operation of these nanodevices, especially NEMS, relies significantly on their high surface-to-volume ratios leading to remarkable size-dependent mechanical properties.[1,11−14] The surface contribution to the overall mechanical behavior increases with decreasing size, thereby resulting in significant size dependence in NW properties.[1,13] For example, the quality factor of Si-based nanoresonators is reduced due to surface loss mechanisms such as adsorption, surface stress, surface oxidation/reconstruction, and surface defects.[1,12,15] The fracture strength is also shown to be strongly correlated to surface-related defects.[13,16] Therefore, a wide range of experimental and computational attempts have been performed to explore Si NW mechanical behavior.[1,12,17−22]

Among experimental techniques, bending tests are ubiquitously employed for the characterization of both elastic and strength properties of Si NWs along with other one-dimensional nanostructures.[1,13,18,23] Bending tests are rather straightforward, where Si NW is loaded preferentially *in situ* with an external force-sensing probe.[21] Similarly, Si NWs can be integrated with testing devices in the form of micro-

Received: May 10, 2023
Accepted: August 8, 2023
Published: August 21, 2023



© 2023 The Authors. Published by American Chemical Society

electromechanical systems (MEMS),[24] where they are exposed to bending loads. The resulting load−displacement data have then to be interpreted through appropriate models.[25] Although there are complicated experimental aspects of bending tests mainly related to nanometrology,[13,17,21,26] the interpretation of test results proved to be the most challenging task, as without a reliable nanomechanical model, the quantification of even the most basic properties such as stiffness and strength becomes an enormous task.[21,23,27−33] The lack of such a sound modeling approach is in fact reflected by a series of conflicting observations including broad range of estimations for elastic and strength properties[1,12] and significant differences between experimental and computational findings.[1,12,18,19,19,20,34,35] Models usually suffer from a poor description of surface-related phenomena[18,20,36] and inconsistent use of constitutive surface models as well as nonlinear elasticity.[1,18,36] In this context, an effective model should involve the implementation of the following three sets of parameters:

(i) Native oxide, essentially amorphous silicon dioxide ($aSiO_2$), is an indispensable part of the Si NW surface[19,20,34,35] and thus affects the NW structure by introducing defects or other interfaces.[37,38] Although usually overlooked, a recent study has revealed tensile intrinsic stresses in Si NWs upon native oxide formation under ambient conditions.[34] Atomistic simulations also exhibit a reduction in the modulus of elasticity of Si NWs to be as much as 40% due to native oxide surface condition while compared to the pristine surface state.[19,20,35] Similar reduction in the ultimate strength is estimated to be up to 20%.[19,20,35]

(ii) Appropriate interatomic potentials for atomistic simulations of surface stress and surface elasticity have to be introduced.[19,35,39] In this regard, surface stress is defined as the reversible work per unit area needed to elastically stretch a pre-existing surface.[20,39] Surface elastic constants represent the variation in bulk elastic constants due to the formation of a surface.[20,39] The classical surface elasticity theory by Gurtin and Murdoch has been widely employed for NWs.[40] Similarly, classical beam theories are extended through considering the surface flexural stiffness[41−43] along with the different surface elasticity models.[32,33,44] However, the results employed to model the bending response[21,23,27,29,32,33,45] have so far delivered various degrees of success for the estimation of size-dependent NW properties.

(iii) Other structural aspects such as finite deformation, intrinsic stresses, and appropriate boundary conditions have to be modeled for mechanical consistency and relevance with respect to experimental conditions.[1,17,18,20,36,39,46] For example, the residual stress effect is embedded in nanomechanical bending models using different formulations,[21,28−30,33] the quantification of which is a subject of high technological demand.[34,47] Uncertainties associated with boundary conditions can also lead to discrepancies due to their direct impact on the load−displacement relationship.[18]

The first two of the three sets of critical parameters listed above are concerned with the state of the NW surface. The effect of the surface on NW flexural deformation is commonly considered via three main approaches: (i) the generalized Young−Laplace linear surface elasticity model (YL),[44] (ii) modified YL,[32,48] and (iii) extended YL.[33] Meanwhile, YL has also been used for extended versions of Timoshenko nanobeams for the inclusion of surface effects.[49] Recently, an ab inito core−shell model based on surface relaxation has been proposed to evaluate the surface effect in the bending of NWs.[50] Due to the challenges and uncertainties associated with obtaining surface properties by experiments,[51,52] these parameters are widely studied via the first principle methods[20,53] and atomistic simulations.[20,39,54] In this regard, the relation between the surface stress and bulk elastic modulus in NWs is revealed using molecular dynamics (MD) simulations.[55,56] The surface condition and crystalline orientation of NW side surfaces can also be crucial for the precision of the nanomechanical model fitted to the experimental data.[21,29,32]

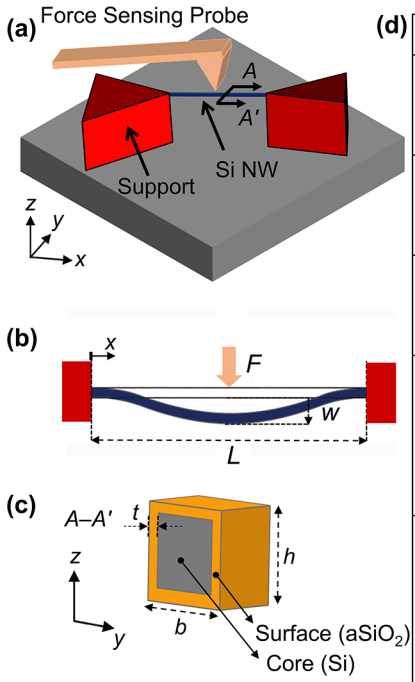
The initial core-surface model by Gurtin and Murdoch[40] is an idealized model as it ignores the surface layer thickness and thus describes the surface as a stretchable but not a bendable structure.[50,57−59] This approach is further improved by a series of core−shell models,[54,58,59] where the NW cross section is considered as a composite structure composed of a bulk core and a surface layer of finite thickness, each with its distinct set of elastic constants.[36,60] The definition of the effective bending rigidity is another cause of further discrepancy among nanomechanical models.[32,33] The term originates from the local geometric nonlinearity of strains through incremental deformation theory.[33,46] Ignoring its dependence on parameters such as surface-induced residual stresses renders YL and modified YL models incapable of capturing surface stress effects emanating from NW side surfaces.[33] These effects are significant upon large deformation of NWs leading to axial reorientations and phase transformations.[33,36] Consequently, the effectiveness of available nanomechanical models[21,23,27−31] in predicting NW bending behavior is directly related to the extent of their parameter sets. Despite progress, anistropic treatment of Si NW surface properties remains as the leading challenge in this field.[20,33,45]

The present work addresses this challenge through a multiscale nanomechanical model. The proposed model is based on extended YL within the Euler−Bernoulli (EB) beam formulation. Addressing the first two of the three critical items mentioned above, the anisotropic implementation of surface stress and surface elasticity is performed for a realistic native oxide surface on Si via atomistic simulations using the reactive force field (ReaxFF).[20] Addressing the last item of structural aspects, the model also accounts for the intrinsic effects induced by both surface stresses and initial residual stresses. The discussion of the model is followed by experimental method, where bending deformation of a Si NW is examined, and its intrinsic stress state is carefully quantified through Raman spectroscopy.[34] Finally, findings are compared to those of prior nanomechanical models in the literature.[21,23,27−30] For this purpose, the force−deflection data obtained through the bending test are used in different models to compute the modulus of elasticity and fracture strength. The paper concludes with a discussion on discrepancies among models, highlighting the importance of developing a multiscale theoretical framework to address size dependence of Si NW mechanical behavior.

MATERIALS AND METHODS

This section introduces the nanomechanical model with its surface- and interface-related aspects. The overall NW architecture and three-

https://doi.org/10.1021/acsanm.3c02077
ACS Appl. Nano Mater. 2023, 6, 15465−15478



(d)

Model	Effective Parameter(s)		Reference
Heidelberg	Large Deflection	T	[23]
Hudson	Large Deflection Intrinsic Stress (Initial Tension/Compression)	σ_0 T	[28]
Zhan	Large Deflection Surface Stress and Surface Elasticity (Modified Young-Laplace)	H T	[29]
Simplified Zare Pakzad (SimpZP)	Large Deflection Intrinsic Stress (Initial Tension/Compression) Surface Stress and Surface Elasticity (Modified Young-Laplace)	H σ_0 T	[21]
Extended Zare Pakzad (ExtZP)	Large Deflection Intrinsic Stress (Initial Tension/Compression and surface-induced residual stress) Surface Stress and Surface Elasticity (Extended Young-Laplace)	$\sigma_0 + \sigma_{xx}$ T $H_{11} + H_{22}$	Current Study

Figure 1. (a) Schematic representation of Si NW, clamped by monolithic support pillars and subjected to a point force applied by a force sensing probe. (b) Schematic of a NW of length L under bending test with applied load F and subsequent deformation w at its center. (c) Cross-sectional representation of the NW with associated height (h), width (b), and native oxide thickness (t). (d) Effective terms of different nanomechanical models. ExtZP exhibits the model introduced in the current study. The terms T and H correspond to the axial tension due to large deflections and surface parameters, respectively, with H_{11} and H_{22} denoting anisotropic surface terms with NW side surfaces treated separately. Intrinsic stress (σ) terms are shown via σ_0 and σ_{xx} representing the residual terms due to initial tension/compression and surface-induced effects, respectively.

point bending test platform are described in Figure 1. Figure 1a depicts a NW between support pillars and loaded at its midspan by a force sensing probe. Figure 1b exhibits a side view with applied load, F, and the resulting midspan deformation, w. A cross-sectional view showing the distinct $aSiO_2$ surface layer is provided in Figure 1c. Based on this background, the modeling approach to the Si NW bending response is introduced next, which is followed by the description of surface properties, including both the unreconstructed surface and native oxide. Finally, experimental methods will be introduced.

Modeling of Nanowire Bending Response. The modulus of elasticity (E) and fracture strength (S) can be predicted by using analytical models based on continuum mechanics. An overview is provided in Figure 1d with the effective parameters associated with each model including large deflection, intrinsic stress, and surface properties schematically described. At the basic level, the linear bending response can be captured using EB beam theory,[61] which was later revised by Heidelberg et al.[23] to include axial stresses due to large deflections, with the axial load denoted by T in Figure 1d. This model was later modified by including intrinsic stresses and surface-related parameters. One such extension regarding intrinsic stresses was introduced by Hudson et al.[28] to account for the initial residual stress, σ_0, due to axial tension/compression loads. This treatment considers all residual stress generation mechanisms due to semiconductor manufacturing processes and manipulation operations for assembly and integration.[62] The modified YL surface model was also incorporated into the Heidelberg model by Zhan et al.,[29] where the surface parameter set is defined by H in Figure 1d.

A recent demonstration by Zare Pakzad et al., the SimpZP model,[21] incorporated both intrinsic stress, σ_0, and surface effects, H, where Raman spectroscopy provided the much needed input for the former parameter. The model proposed in the present work, the ExtZP model, represents a significant multiscale extension of the SimpZP model, where the treatment of the surface is enhanced by incorporating two new sets of effective parameters as exhibited in Figure 1d: (i) anisotropic surface parameters, H_{11} and H_{22}, and (ii) surface-induced residual stresses, σ_{xx}. In the upcoming section, the computation of surface stresses and surface elastic constants will be elucidated using atomistic simulations. Hence, ExtZP represents the most general approach for the interpretation of the Si NW bending response. Its governing equation for a NW of length L and of rectangular cross section loaded at its midsection by a point load F (Figure 1a,b) is given in eq 1.

$$(EI)^*\frac{\partial^4 w}{\partial x^4} - T\frac{\partial^2 w}{\partial x^2} - H\frac{\partial^2 w}{\partial x^2} = \frac{F}{2}\left(-\delta(x) + 2\delta\left(x - \frac{L}{2}\right) - \delta(x - L)\right) \quad (1)$$

where w is the transverse displacement in the z-direction, x denotes NW longitudinal axis, E is the modulus of elasticity, I is the moment of inertia, $(EI)^*$ is the effective flexural rigidity, T is the overall tension along the NW, δ is the Dirac delta function, and H is the surface parameter. H is defined as $H = H_{11} + H_{22} + bh\sigma_{xx}$, where σ_{xx} is the surface induced residual stress and h and b are the NW thickness and width, respectively. With terms H_{11} and H_{22} defined as effective surface terms embedding the surface constants and geometrical representation of involved side surfaces,[33,39] eq 1 can be further modified (eq 2).

$$(EI)^*\frac{\partial^4 w}{\partial x^4} - T\frac{\partial^2 w}{\partial x^2} - 2hf_{11}\frac{\partial^2 w}{\partial x^2} - 2bf_{22}\frac{\partial^2 w}{\partial x^2} - 2hd_{11}\frac{\partial^2 w}{\partial x^2} - 2bd_{22}\frac{\partial^2 w}{\partial x^2} - bh\sigma_{xx}\frac{\partial^2 w}{\partial x^2} = \frac{F}{2}\left(-\delta(x) + 2\delta\left(x - \frac{L}{2}\right) - \delta(x - L)\right) \quad (2)$$

where the indices 11 and 22 denote the corresponding directions for the involved planar surfaces. The first term in eq 2 with four spatial derivatives is related to bending and resulting transverse deflections, while the second term represents the effect of axial tension. The components of the overall tension term, T, are given in eq 3

https://doi.org/10.1021/acsanm.3c02077
ACS Appl. Nano Mater. 2023, 6, 15465−15478

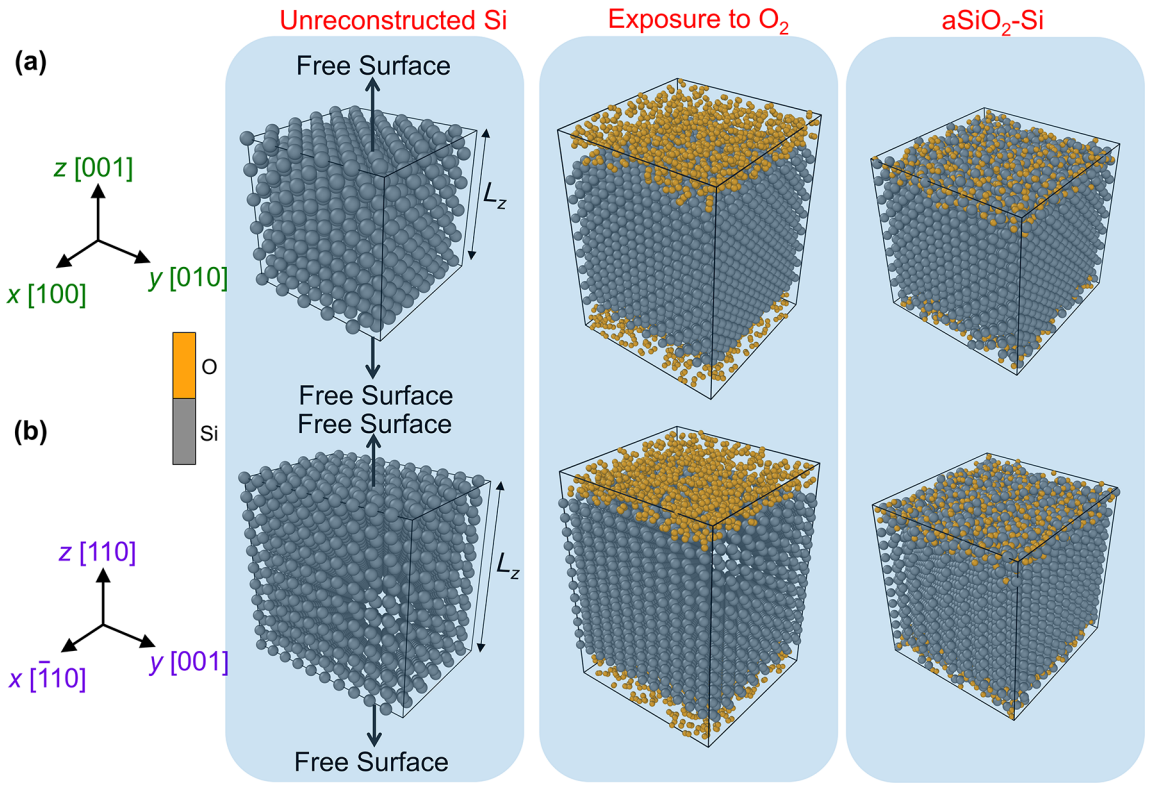


Figure 2. Atomic configurations for the initial unreconstructed Si thin film (left), its exposure to oxygen (middle), and the oxidized Si (right) with (a) (100) and (b) (110) free surfaces in the *z*-direction. Si and O atoms are shown with gray and orange spheres, respectively.

$$T = T_0 + \frac{EA}{2L}\int_0^L \left(\frac{\partial w}{\partial x}\right)^2 \mathrm{d}x \tag{3}$$

where T_0 is the residual force due to initial tension/compression in the NW and the second term represents axial tension due to large deflections. Finally, A denotes the NW cross-sectional area. The next five terms in eq 2 represent the surface effect via surface stress components (f_{11} and f_{22}), surface elasticity constants (d_{11} and d_{22}), and surface-induced residual stress (σ_{xx}). The details and formalism regarding the treatment of surfaces and interfaces will be discussed in the next section.

Equations 2 and 3 are solved subject to the usual clamped boundary conditions at both ends of the NW, resulting in the solution given in eq 4.

$$F = \frac{192EI}{L^3} w\left(\frac{L}{2}\right) f(\alpha) \tag{4}$$

This equation is reduced to the linear EB beam deflection approximation in the case of $f(\alpha) = 1$. An exact solution method results in the formulation of eq 5.[23]

$$f(\alpha) = \frac{\alpha}{48 - \frac{192\tanh(\sqrt{\alpha}/4)}{\sqrt{\alpha}}} \tag{5}$$

To find the ultimate strength of the material (S), the maximum stress analysis for NW at fracture results in the formulation of eq 6.[27]

$$S = \frac{FL}{2\pi R^3} g(\alpha) \tag{6}$$

where R is the equivalent NW radius. $g(\alpha)$ of eq 6 is given in eq 7.

$$g(\alpha) = \frac{4}{\sqrt{\alpha}}\tanh\left(\frac{\sqrt{\alpha}}{4}\right) + \left(\frac{2 + \cosh\left(\frac{\sqrt{\alpha}}{2}\right) - 6\frac{\sinh\left(\frac{\sqrt{\alpha}}{2}\right)}{\sqrt{\alpha}}}{\alpha\cosh^2\left(\frac{\sqrt{\alpha}}{4}\right)}\right)^{1/2} \tag{7}$$

where α is related to the maximum deflection by the following transcendental equation and is used for both $f(\alpha)$ and $g(\alpha)$ terms needed for E and S calculations. The exact solution for the nanomechanical model is given in eq 8.

$$\left(1 - \frac{L^2T_0}{\alpha(EI)^*}\right)\left(\frac{(EA)^*}{T_0 + (EA)^*}\right)\left(1 - \frac{L^2H_{11}}{\alpha(EI)^*}\right)\left(1 - \frac{L^2H_{22}}{\alpha(EI)^*}\right)\left(\frac{\alpha\cosh^2\left(\frac{\sqrt{\alpha}}{4}\right)}{2 + \cosh\left(\frac{\sqrt{\alpha}}{2}\right) - 6\frac{\sinh\left(\frac{\sqrt{\alpha}}{2}\right)}{\sqrt{\alpha}}}\right)\left(1 - 4\frac{\tanh(\sqrt{\alpha}/4)}{\sqrt{\alpha}}\right)^2 = \Delta Z_{\text{center}}^2\left(\frac{(EA)^* + 2hd_{11} + 2bd_{22} + bhE^*}{(EI)^*}\right) \tag{8}$$

The formulation given in eq 8 provides the solution for the calculation of effective modulus of elasticity (E^*) and S. For the E estimation, the relation between classical bending rigidity and effective bending rigidity as a function of surface properties and geometrical definitions is used. Equation 9 provides the formulation for the effective bending rigidity using the extended YL approach implemented with the ExtZP model of this work.

$$(EI)^* = EI + (E_s + \tau_0)\left(\frac{bh^2}{2} + \frac{h^3}{6}\right) \tag{9}$$

In this formulation, the average surface stresses (f_{11} and f_{22}) and surface elasticity constants (d_{11} and d_{22}) are denoted as τ_0 and E_s, respectively. E_s and τ_0 are often termed the surface modulus and initial surface stress, respectively, in the literature of nanomechanical models.[32] Further details on the formulation of prior models[21,23,28,29] and related bending rigidity formulations[32,33,48] can be found elsewhere.

Overall, this formulation achieves an all-inclusive theoretical framework with significant improvements related to the interpretation of bending deformation in Si NWs. This is achieved first due to the

https://doi.org/10.1021/acsanm.3c02077
ACS Appl. Nano Mater. 2023, 6, 15465−15478

Table 1. Dimensions, Number of Atoms, and Evaluation Areas of Thin Film Structures for Unreconstructed Si and $aSiO_2$−Si Structures with Associated Crystallographic Orientations of the Si Core

	Si orientation			dimensions [nm]			no. of atoms		
structure	x	y	z	x	y	z	Si	O	A_{film} [nm^2]
Si (100)	[100]	[010]	[001]	4.35	4.35	4.35	4224		37.8
Si (110)	[$\bar{1}$10]	[001]	[110]	6.15	4.35	6.15	8448		53.5
$aSiO_2$−Si (100)	[100]	[010]	[001]	4.35	4.35	4.50	4096	976	37.8
$aSiO_2$−Si (110)	[$\bar{1}$10]	[001]	[110]	4.35	4.61	4.61	4608	1158	40.1

incorporation of the extended YL surface model[33] and initial tension/compression terms into the analysis of Si NW bending test data. Second and more importantly, anisotropic treatment of NW surfaces and the resulting stiffening/softening aspects of native oxide surface are fully implemented. The technique developed for the calculation of the associated surface properties is introduced in the next subsection.

Surface and Interface Analysis. This section covers surface- and interface-related aspects of the ExtZP model. MD simulations are employed to calculate surface stresses and surface elastic constants for Si crystal surfaces that are either unreconstructed or coated with a native oxide layer. The details of generating the native oxide structures with the subsequent MD approach for the calculation of surface properties are detailed next.

Native Oxide Model. Oxidation processes are modeled at the atomic scale by using reactive MD simulations. For this purpose, ReaxFF is employed with LAMMPS.[63] The ReaxFF potential uses the concept of partial bond orders to accurately model bond breaking and bond formation, approaching quantum mechanical accuracy.[64] The approach was previously employed to study the effects of temperature, size, and stress on the oxidation of Si NWs.[34,65,66] A detailed description of the force field developed for the Si/SiO_2 system can be found elsewhere.[64] This approach is proven to deliver reliable process modeling as a function of temperature and defect generation.[66] In this work, the force field parameters developed by Newsome et al.[67] are used to model Si crystal blocks as shown in Figure 2. Periodic boundary conditions (B.C.s) are applied along x- and y-directions, while a nonperiodic boundary condition is applied along the z-direction to mimic a two-dimensional structure, i.e., a thin film, with free surfaces. The unreconstructed Si surfaces with (100) and (110) orientations, as shown in Figures 2a and 2b, respectively, are considered as the starting point. These models are built with crystal orientations of (x, y, z) = ([100], [010], and [001]) and (x, y, z) = ([$\bar{1}$10], [001], and [110]) using 4096 and 4608 Si atoms, respectively. The coordinates of incident molecules of oxygen (O_2) are randomly placed on both sides of Si thin films with a total number of 800 O_2 molecules, as depicted in the middle column of Figure 2. A benchmark examination is performed to determine the appropriate number and distribution of the O_2 molecules on the upper and lower surfaces of Si thin film models. At first, the simulation box is relaxed at a temperature of 25 °C and under a pressure of 1 atm for 300 ps using isobaric ensemble (NPT) with a time step of 1 fs. The final configurations of Si structures with native oxide surface are denoted as $aSiO_2$−Si (last column of Figure 2) in the remainder of this work and will be used for the calculation of surface properties, as explained next.

Calculation of Surface Properties. The reason behind the present spread of stiffness and strength values in the literature can mainly be traced back to the lack of a proper theoretical treatment of surface mechanics. Despite numerous atomistic,[20,39,68−70] density functional theory (DFT),[53,56,71,72] finite element (FE),[73−77] and experimental[52] studies on Si surface constants, a consensus on surface stress profiles and subsequent calculation of constants for different crystalline orientations and surface conditions is still missing. To quantify Si NW surface stress components, f_{11} and f_{22}, and surface elastic constants, d_{11} and d_{22}, in both (100) and (110), Martin's method[39] can be applied to the thin film structures of Figure 2. As periodic B.C.s are applied in x- and y-directions only, an infinite film model with finite thickness (L_z) in the z-direction is achieved as shown in Figure 2. The evaluation area (A_{film}) consists of two free surfaces that face each other, where the film must be thick enough to prevent the interaction of the two free surfaces. Involved dimensions, crystallographic orientations, numbers of atoms, and evaluation areas for unreconstructed Si and $aSiO_2$−Si models are listed in Table 1.

To quantify surface stress components, structures are first equilibrated at 0.01 K by using NPT dynamics. Subsequently, the total energy is minimized using the steepest descent and conjugate gradient techniques. By assuming a film thickness of L_z, the surface stress components are formulated as shown in eq 10, where η represents the averaged strain due to the relaxation.

$$f_{ij}(\eta) = f_{ij}^{film}(\eta) - f_{ij}^{bulk}(\eta) \tag{10}$$

Bulk surface stress must be estimated separately by the bulk model and surface stress for the film model can be defined by using the stress tensor definition, σ_{ij}^{film}, given in eq 11. Further details about the stress tensor of thin films can be found elsewhere.[39]

$$f_{ij}^{film}(\eta) = \sigma_{ij}^{film}(\eta)\frac{L_z}{2} \tag{11}$$

Similarly, surface elastic constants (d_{ijkl}) are defined as second-order derivatives of the surface energy with respect to strain under the plane-stress conditions highlighted in Figure 2. The usual elastic constants for bulk (C_{ijkl}^{bulk}) and film (C_{ijkl}^{film}) models are calculated using MD simulations, while, for the bulk model, the elastic constants should be defined under plane-stress condition ($C_{ijkl}^{bulk,plane}$) using the relations given in eqs 12, 13, and 14.[39]

$$C_{11}^{bulk,plane} = C_{11} - \frac{C_{13}^{\ 2}}{C_{33}} \tag{12}$$

$$C_{22}^{bulk,plane} = C_{22} - \frac{C_{12}^{\ 2}}{C_{33}} \tag{13}$$

$$C_{12}^{bulk,plane} = C_{12} - \frac{C_{12}C_{13}}{C_{33}} \tag{14}$$

The relationship between the plane-stress elastic constants of the bulk and film models with the surface elastic constants is represented in eq 15.[39]

$$C_{ijkl}^{film,plane} = C_{ijkl}^{bulk,plane} - \frac{2}{L_z}d_{ijkl} \tag{15}$$

The Tersoff−Munetoh potential[78] as an empirical function composed of two-body terms depending on the local environment is used for the calculation of surface properties in this work. To obtain elastic constants, infinitesimal strains are applied to the simulation box in different directions, and the resulting variation of the energy is measured. The associated thin film stress state, π_{ij}, is calculated using the virial theorem,[79] given in eq 16.

$$\pi_{ij} = \frac{1}{2\Omega_0}\left[\sum_{\alpha=1}^{N}\sum_{\beta\neq\alpha}^{N}\frac{1}{r^{\alpha\beta}}\frac{\partial V(r^{\alpha\beta})}{\partial r}(v_i^{\alpha\beta}v_j^{\alpha\beta})\right] \tag{16}$$

where Ω_0 stands for the atomic volume in an undeformed system with N as the total number of atoms where associated atomic volumes for Si and SiO_2 are calculated via relaxation of related structures in each crystallographic direction with further details given in ref 20. Atomic distances between atoms α and β are represented as $r_{\alpha\beta}$. v_j^{α} stands for

https://doi.org/10.1021/acsanm.3c02077
ACS Appl. Nano Mater. 2023, 6, 15465−15478

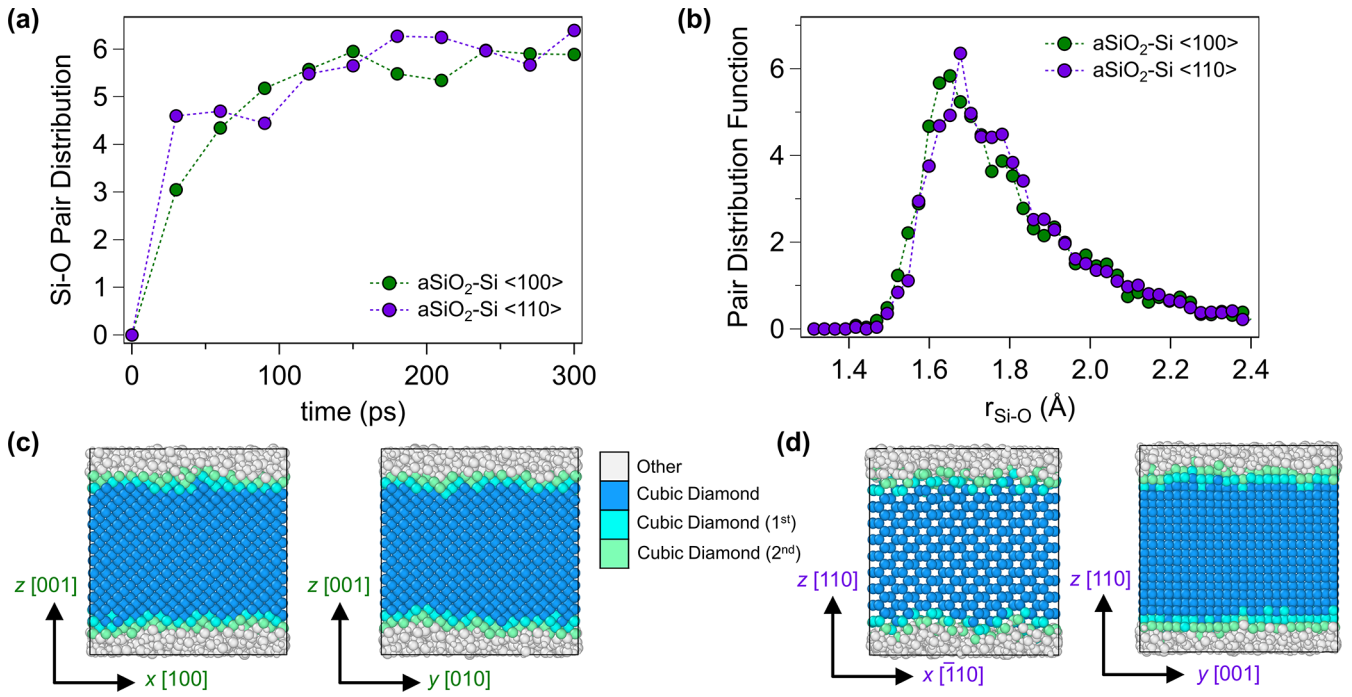


Figure 3. (a) Magnitude of the Si−O pair distribution as a function of time for $aSiO_2$−Si thin films. (b) PDF of Si−O for Si NWs at 300 ps. For each $aSiO_2$−Si structure with (c) (100) and (d) (110) free surfaces, the side surfaces are shown with associated color codes representing diamond cubic structure analysis results. The color bar indicates the amorphous and cubic diamond structures with related first and second neighbors.

the position of atom α along the j direction; i.e., $v_j^{\alpha\beta} = v_j^{\alpha} - v_j^{\beta}$, and V represents the interatomic potential.

Experimental Methods. The particular bending test approach of Figure 1a introduces ample space between the NW specimen and the substrate, thereby allowing large out-of-plane deflections.[21,25] Si NW is thus subjected to a point force applied by a force sensing probe. As both the Si NW specimen and the microscale supports are fabricated monolithically within the same crystal, there are no interface effects, such as those encountered in pick-and-place assembly or vapor−liquid−solid (VLS)-based synthesis work, that would cause ill-defined mechanical B.C.s in the present bending architecture. This structure was achieved by using a top-down fabrication technology developed specifically for Si NW integration in MEMS.[22,25,80] The process flow is based on a combination of shallow and deep etch processes for the definition and release of Si NW, respectively, with the resulting NWs subjected to a series of structural studies.[22,25,34,81] Si NWs of this work are patterned with a line width of 80 nm along the ⟨110⟩ direction on a p-type ⟨100⟩ Si wafer. Further details associated with the fabrication approach can be found elsewhere.[21,22,25,34,80] A series of transmission electron microscopy (TEM) images obtained through focused-ion beam (FIB) milling reveal the cross-sectional features of the Si NW.[21,22,25,34,80]

The *in situ* three-point bending test is performed within the vacuum chamber of dual-beam FIB/SEM equipment at ambient temperature. A micromanipulator equipped with a piezoresistive cantilever-based Kleindiek force sensor is used to measure the applied load, F, while the bending deflection, w, is quantified through image analysis of micrographs. Upon contact with the test sample, the piezoresistive gage produces an analogue voltage output, which is converted into a force value according to a former calibration step and recorded with a sampling period of 1 s. An image correlation software (VEDDAC6) is used in pixel-level precision for each force measurement. Loading is continued until fracture. Further details related to the three-point bending method can be found elsewhere.[21,25,34]

For the interpretation of the F−w data obtained from the bending test, one needs to assess the total uniaxial intrinsic stress, σ, due to two residual stress components generated in the Si NW: (i) the initial tension/compression force, T_0, and (ii) surface-induced residual stress, σ_{xx}. σ is quantified via Raman spectroscopy in a home-built μ-Raman setup equipped with a Princeton Instrument SP-2500 spectrometer. In this measurement, a laser beam of 488 nm wavelength is used as an excitation source with a spot size of 1 μm achieved through a beam splitter and microscope objective lenses. An integrated microscope with the measurement setup is used to focus the microspot on the NW. This facilitates a line scanning system to analyze the Raman shift along the entire length of suspended Si NWs with a high spatial resolution. The Raman shift ($\Delta\omega$) can be related to the uniaxial intrinsic stress along the NW using the stress shift coefficient (SSC).[82] A broad range of SSC is reported for Si NWs, where the SSC of -1.93×10^{-9} cm^{-1} Pa^{-1} is recommended for NWs for sub-100 nm thickness.[82] Therefore, the relation given in eq 17 is used for the intrinsic stress, σ, calculation, where S_{11} and S_{12} are the elastic constants and p and q are the phonon deformation profiles. Further details related to the calibration of the laser power, Raman analysis, and the determination of related constants can be found elsewhere.[21,34,82]

$$\Delta\omega = \frac{1}{2\omega_0}[pS_{12} + q(S_{11} + S_{12})]\sigma = (\mathrm{SSC})\sigma$$
$$= -1.93 \times 10^{-9} \times (\sigma\ [\mathrm{Pa}]) \quad (17)$$

RESULTS AND DISCUSSION

This section starts with the determination of surface parameters, including surface stresses and surface elasticity constants for both unreconstructed and native oxide surfaces. This is followed by the characterization of the bending response of a Si NW. The resulting force−deflection relationship is then interpreted to extract the modulus of elasticity and strength of the Si crystal. These results are compared and contrasted with those obtained by the existing models from the literature.

Surface Properties. The modeling of oxidation on (100) and (110) crystalline Si surfaces was already introduced in Figure 2, where free surfaces exposed to oxygen are defined in

https://doi.org/10.1021/acsanm.3c02077
ACS Appl. Nano Mater. 2023, 6, 15465−15478

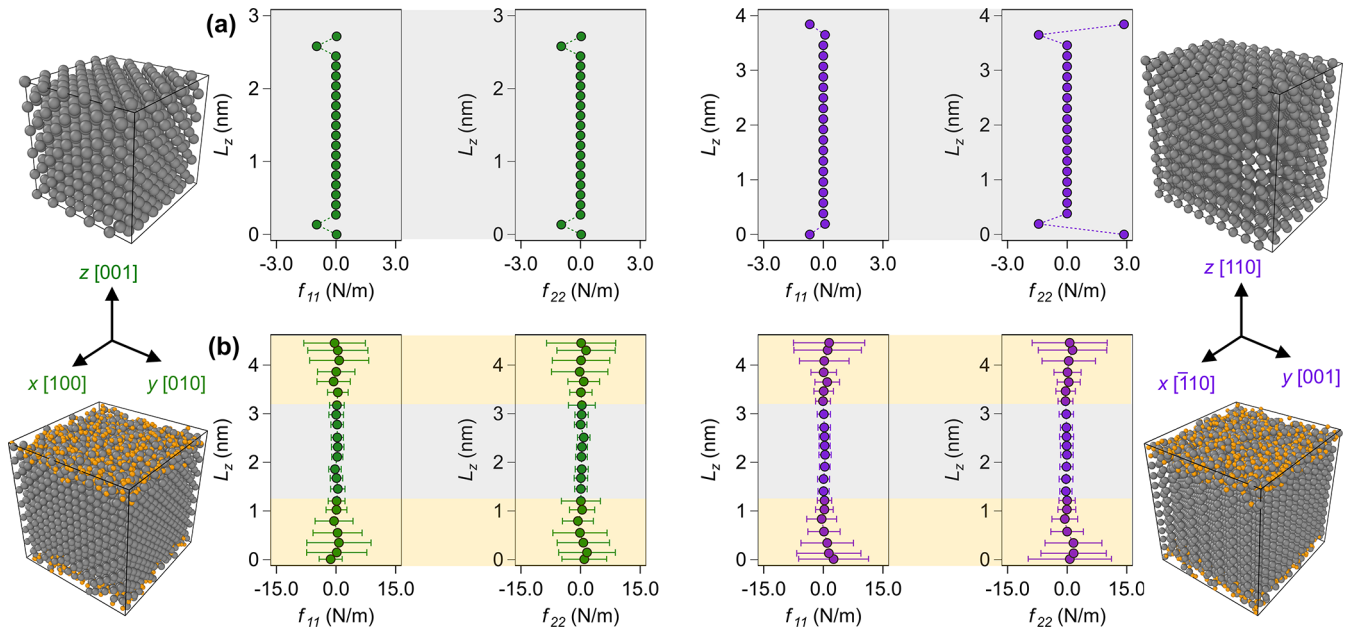


Figure 4. Atomic stresses for (a) unreconstructed Si and (b) $aSiO_2$−Si film structures with (100) and (110) free surfaces of the crystalline Si core. The stress components, f_{11} and f_{22}, are shown for each of the atomic structures studied here.

Table 2. Surface Stress and Surface Elastic Constants for Unreconstructed Si and $aSiO_2$−Si Structures with Associated Crystallographic Orientations of the Crystalline Si Core

	surface properties [N/m]			
structure	f_{11}	f_{22}	d_{11}	d_{22}
Si (100)	−0.88	−0.88	−8.77	−8.77
Si (110)	−1.57	−0.95	+3.40	−15.10
$aSiO_2$−Si (100)	−2.57 ± 0.15	−2.57 ± 0.15	−7.16 ± 1.24	−7.16 ± 1.24
$aSiO_2$−Si (110)	−6.33 ± 0.50	−4.90 ± 0.50	+9.05 ± 3.51	+47.82 ± 4.01

the z-direction. The atomic snapshots in the last column, $aSiO_2$−Si, exhibit the outcome of this process at room temperature. The oxide formation on Si surfaces is studied first through measuring the pair distribution functions (PDFs) to characterize the arrangement of distances between pairs of particles within a specific volume. Figure 3 demonstrates the magnitude of the pair distribution for Si−O bonds over the simulation time. Oxidation occurs with a high rate within the first 30 ps and then reaching a steady-state condition after 90 ps. Figure 3b depicts the PDF of Si−O bonds at 300 ps as a function of the bond length (r_{Si-O}). A peak at 1.70 Å is observed for the PDF of oxide. The average Si−O bond length of 1.60 Å has been reported previously using MD simulations.[34,83,84] Similarly, the native oxide thickness is measured using the diamond crystal structure analysis while identifying Si core and native oxide regions.[85] Figures 3c and 3d demonstrate the diamond cubic crystal in Si core in x−z and y−z cross sections for (100) and (110), respectively, while an amorphous native oxide layer is formed on the upper and lower surfaces. Results indicate a native oxide thickness ranging between 0.5 nm and 0.7 nm encapsulating the Si crystal, which is comparable to previous experimental observations[37,86] as well as MD simulations.[34,38,65]

Once atomistic configurations for crystalline Si with and without a native oxide layer on the free surface are generated successfully, the calculation of surface constants is the subsequent step. The method for obtaining surface properties as discussed before is applied to nanoscale thin films of unreconstructed Si and $aSiO_2$−Si depicted in Figure 2 and listed in Table 1. The surfaces are relaxed using the conjugate gradient method for the calculation of the surface stress and surface elastic constants. The applicability of this method was previously examined on pure Si surfaces using different interatomic potentials which provided good agreement with prior MD and DFT studies on surface properties of Si thin films.[20,39,68,69,87]

Stresses obtained according to eq 16 are depicted in Figures 4a and 4b for unreconstructed Si and $aSiO_2$−Si thin films, respectively. Stress profiles of Figure 4a demonstrate stress variation within only 2 to 3 atomic layers in the proximity of the free unreconstructed Si surface. This finding agrees well with prior reports on unreconstructed Si surfaces.[39,71] With the modeling approach thus validated, the objective behind the modeling of the unreconstructed Si thin film is achieved. On the other hand, for $aSiO_2$−Si thin films of Figure 4b, a significant stress variation is observed within 5 to 6 atomic layers colored with yellow in the plots. The distribution of stresses in the bulk crystal and free surface zones is also comparable to those in prior reports.[20,39,53,71] While stress estimations range between −3 and +3 N/m for unreconstructed Si film structures, this changes from −12 to +12 N/m for $aSiO_2$−Si films. The ability thus achieved to quantify surface stresses will provide further insight into native oxide growth[88,89] and associated stiffening/softening effects due to changes in surface constants.[20,39,53,71]

https://doi.org/10.1021/acsanm.3c02077
ACS Appl. Nano Mater. 2023, 6, 15465−15478

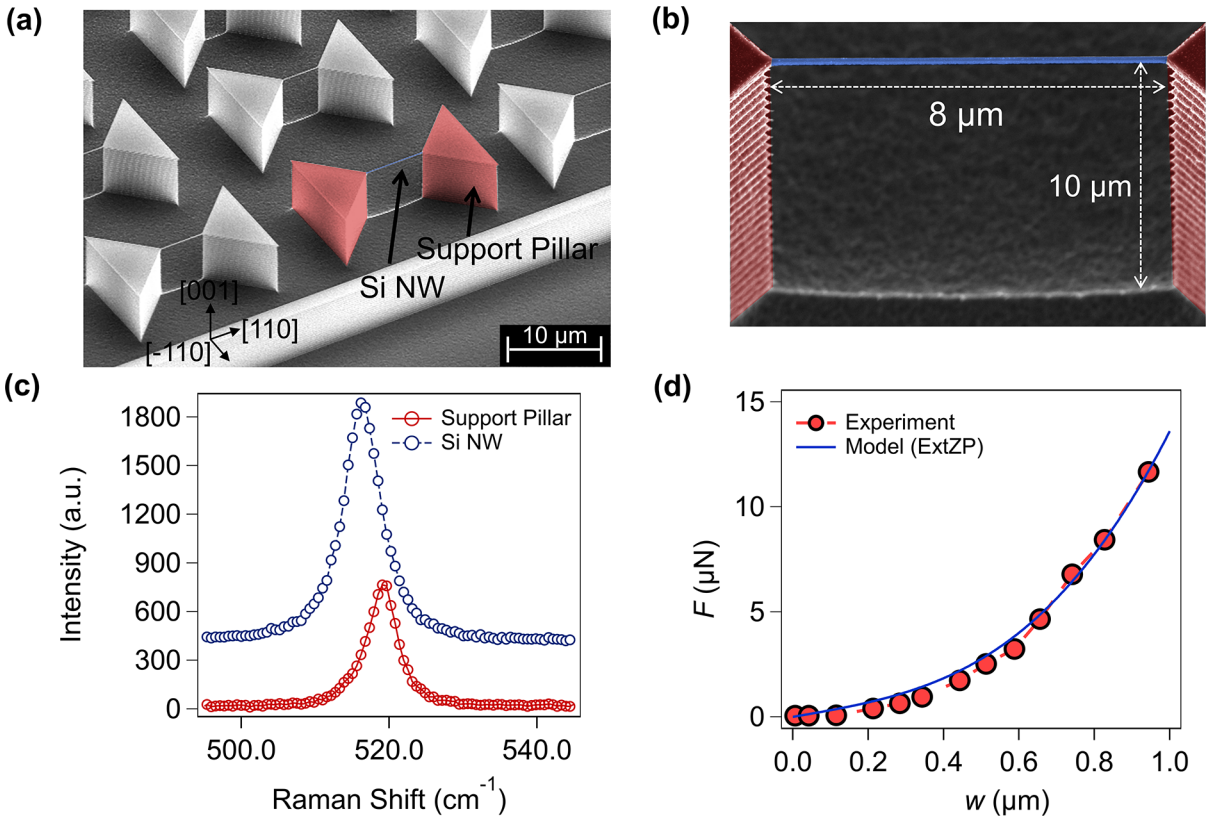


Figure 5. (a) Scanning electron micrograph of suspended Si NWs between support pillars. (b) Close-up micrograph showing dimensions and trench. (c) Raman spectra measured through a line on the support pillar and Si NW. (d) $F-w$ data obtained through a three-point bending test and fitted curve using the ExtZP nanomechanical model.

Having observed stress profiles within the immediate proximity of oxide surfaces, surface stress components, f_{11} and f_{22}, and surface elastic constants, d_{11} and d_{22}, are calculated using eqs 11 and 15, respectively, and tabulated in Table 2. The variation of surface properties is obtained with the evolution of stress and elastic components along the film thickness tracked. In this respect, calculated surface properties can be compared to those of previous studies on unreconstructed and oxidized Si thin films.[20,39,68,73−77] The surface stress and surface elastic constants calculated for unreconstructed (100) and (110) Si surfaces are in perfect agreement with prior MD[20,39,68,70] and DFT[56] reports modeled via different interatomic potentials. Despite the differences between the atomistic approaches, the surface elastic constants for unreconstructed (100) Si films also match well with Miller and Shenoy's constants.[54] Moreover, the surface stress constants obtained for unreconstructed (100) Si surface are in a good agreement with the predictions of prior FE studies.[73−77]

Similarly, $aSiO_2$−Si surface constants are compared to those found in a limited number of reports. Prior DFT studies on oxidized (100) Si surface reported compressive surface stresses ranging between 3.2 and 4 N/m depending on the structure of native oxide.[72] The surface stress constants given as f_{11} and f_{22} in Table 2 for $aSiO_2$−Si (100) are of the same sign and are in close range. The average of the surface stress components, f_{11} and f_{22}, reported as 10.3 N/m in compression by Melis et al.[53] agrees well with those for $aSiO_2$−Si (110) given in Table 2. Considering vastly different computational approaches employed for the calculation of surface properties, the deviations observed between the predictions are quite acceptable.[20,38,53,69,71−73] The surface properties including surface stress components (f_{11} and f_{22}) and surface elastic constants (d_{11} and d_{22}) given in Table 2 are presented graphically in Figure S2.

In summary, Table 2 demonstrates a set of significant differences in surface mechanics introduced by oxidation. It is interesting to see that the presence of oxide also amplifies anisotropic effects, as properties such as f_{22} and d_{22} become even more orientation sensitive compared to unreconstructed Si surfaces. Therefore, it is clear that any interpretation of mechanical testing on Si NWs should incorporate the surface state with precise chemistry and crystal orientation. The constants listed in Table 2 are derived using the described method in this study, and the obtained results are verified through energy-based calculations. The objective of the findings presented here is to establish a standardized approach by considering different surface states or crystallographic orientations rather than providing a mere case study. This approach aims to address the need for revisiting the previously reported scattered constants obtained by using various methods and interatomic potentials. By providing a standardized framework, this study provides a guideline to characterize the surface properties of Si.

The greater surface constants obtained in this study for $aSiO_2$−Si structures, when compared to unreconstructed Si films, provide an explanation for the findings reported by Pennelli et al.[52] Table 2 shows that the surface constants for $aSiO_2$−Si structures are more consistent with the experimental results[52] than the frequently performed comparison with pure Si surfaces.[56,70] Despite the difference in Si orientation, the observed increase in surface stresses of Si structures due to

https://doi.org/10.1021/acsanm.3c02077
ACS Appl. Nano Mater. 2023, 6, 15465−15478

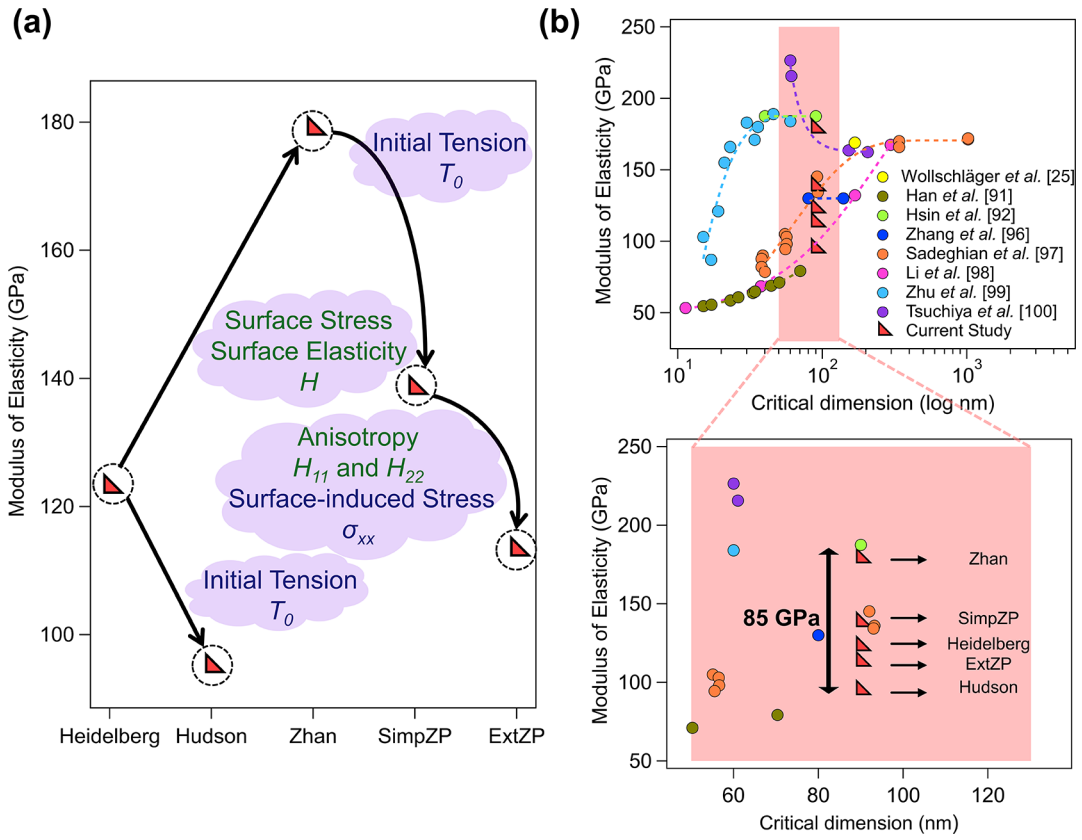


Figure 6. (a) Modulus of elasticity predictions for each nanomechanical model. Arrows indicating trends are accompanied by effective terms involved in each case. (b) A comparison of the predictions of (a) with the literature reporting the modulus of elasticity for top-down ⟨110⟩-oriented Si NWs. The inset shows the distribution of modulus of elasticity predictions within a narrow zone between 50 and 130 nm of critical NW dimension. The scatter due to the use of different models for the interpretation of a single test data is 85 GPa, a significant value that questions the physical nature of the scatter reported previously.

oxidation as highlighted by the data in Table 2 is also in alignment with prior experimental determination of adsorbate-induced surface stress on (111) Si surfaces.[90] The significant compressive f_{11} and f_{22} components obtained for $aSiO_2$−Si can be traced back to the mismatch between the native oxide and crystalline Si lattice constants.[53] The strong dependence of surface properties on oxidation conditions such as the temperature, time, and crystallographic orientation is also consistent with previous reports in the literature.[20,52,72]

Si NW Bending Response. The particular ⟨110⟩ Si NW as the test specimen of this study is shown in Figure 5a, a close-up of which is provided in Figure 5b. The close-up demonstrates the monolithic nature of the architecture, with an etch depth of 10 μm and a NW length of 8 μm. The cross-sectional analysis of Si NW was performed using the FIB milling process, followed by TEM imaging, as reported previously in ref 21. The Si NW cross section is found to be of a trapezoidal shape with a height of 70 nm and a width increasing from 90 nm at the top NW surface to 98 nm at the bottom.[21] A conformal native oxide layer with a thickness of 3 nm is also observed.[21,25]

After measuring NW dimensions, Raman spectroscopy is employed to measure Si NW intrinsic stress, σ, of eq 17. For this purpose, line scans are taken along both the Si NW and support pillars, the latter representing bulk measurement. Figure 5c shows the results of such line scans, where Raman shifts of 519.0 and 517.5 cm^{-1} are obtained for the support pillars and Si NW, respectively, resulting in a downshift of 1.5 cm^{-1}. Thus, a tensile stress of 789 MPa is measured via the Raman shift formulation of eq 17. Further insights into the determination of stress arising from the formation of native oxide and comparable computational investigations involving intrinsic stresses utilizing reactive MD can be found elsewhere.[34] Finally, the bending response of the Si NW characterized through an *in situ* three-point bending test is shown in Figure 5d in the form of a F−w curve. It exhibits a nonlinear response with a force range up to 12 μN and associated midpoint deflection ranging up to 1 μm. Note that this deflection is almost 15 times larger than the NW height, thereby necessitating nonlinear formulation. The ExtZP model is then fitted to the experimental data to estimate E and S. For this purpose, surface stress components (f_{11} and f_{22}) and surface elasticity constants (d_{11} and d_{22}) for $aSiO_2$−Si (110) listed in Table 2 are used as surface constants. The resulting fit curve is also shown in Figure 5d. The force−deflection fit provided in Figure 5d is obtained with the ExtZP model by considering the native oxide surface state, i.e., $aSiO_2$−Si (110), with the corresponding parameters listed in Table 2. Estimated stiffness and strength values for the Si NW and their interpretation are provided next.

Interpretation of Test Results. In addition to the ExtZP model of this work, the F−w response of Figure 5d is examined via a series of other models as mentioned in Figure 1d, and the predictions for E are tabulated in Figure 6a. The resulting fit curves via the Heidelberg, Hudson, Zhan, and SimZP models are given in Figure S1. First of all, considering midpoint deflections exceeding the NW height by at least 1 order of

https://doi.org/10.1021/acsanm.3c02077
ACS Appl. Nano Mater. 2023, 6, 15465−15478

magnitude, large deflections (Heidelberg model[23]) have to be accounted for with the resulting tensile load, T, along the NW axis. This approach yields a modulus of elasticity of 123 GPa. Incorporating an extra term for the initial tension, T_0, according to the Hudson model[28] decreases E to 95 GPa. On the contrary, if Raman results yielded a compressive intrinsic stress, the estimated modulus of elasticity would have increased. If, instead of initial tension, surface parameters, f_{11} and d_{11}, are taken into account according to the Zhan model,[29] E is increased to 178.9 GPa. With the SimpZP model embedding both the initial tension, T_0, and surface parameters, f_{11} and d_{11}, into the formulation, E is estimated as 138.4 GPa. Finally, using the ExtZP model developed in the current study, E is reduced to 113.2 GPa, as all related parameters including anisotropic surface stresses, f_{11} and f_{22}, surface elastic constants, d_{11} and d_{22}, and surface-induced residual stress, σ_{xx}, are taken into account. Findings for E along with those regarding E^* (if applicable) with all models of Figure 1d are listed in Table 3. A comparison of E with other top-down studies on ⟨110⟩-oriented Si NWs is provided in Figure 6b. Despite similar dimensions and crystalline orientation, no clear trend is exhibited by this overview of the literature. Some estimations, e.g. by Han et al.[91] and Hsin et al.,[92] differ by as much as three times. The inset further depicts the distribution of modulus of elasticity estimations in close proximity of the particular NW critical dimension of this study, where predictions of all five models of Figure 1d obtained on single test data are highlighted with an 85 GPa peak-to-peak variation. This perspective shows how critical the modeling is in the interpretation of NW bending response.

Table 3. Effective Modulus of Elasticity (E^*), Modulus of Elasticity (E), and Fracture Strength (S) Estimations Using Different Nanomechanical Models for the Si NW Studied Here

property	Heidelberg[23,27]	Hudson[28]	Zhan[29]	SimpZP[21]	ExtZP (this study)
E^* [GPa]	N/A	N/A	126.0	99.0	85.0
E [GPa]	123.0	95.0	178.9	138.4	113.2
S [GPa]	8.4	7.8	8.5	10.5	7.2

Based on the same test data, a similar deviation between strength, S, estimations by different models is obtained. According to Table 3, S estimations range from 7.8 to 10.5 GPa according to Hudson and SimpZP models, respectively, an appreciable 2.7 GPa difference. This stems from the utilization of various combinations of surface and intrinsic terms in different models, as illustrated in Figure 1d. They enter the formulation through the correction factor, $g(\alpha)$, of eq 6. For example, implementing an initial tension, T_0, in the Hudson model[28] reduces S from 8.4 GPa, as predicted by the Heidelberg model,[23] to 7.8 GPa. It recovers back to 8.5 GPa, when H is considered according to the Zhan model.[29] The prediction for S increases to 10.5 GPa, when the SimpZP model incorporates both of the aforementioned terms of Hudson and Zhan models. Finally, the surface treatment of ExtZP model provides a fracture strength of 7.2 GPa. In this context, the ExtZP model demonstrates the lowest fracture strength compared to all other models considered in this study. The ExtZP model stands out as the only model that integrates the entire set of the surface properties, encompassing surface stress, surface elastic constants, and intrinsic stresses. There are other parameters, such as surface defects, influencing the fracture strength,[13] which needs further investigation in the development of nanomechanical models. Considering strength estimations for Si NWs ranging from a few MPa to 20 GPa in the literature,[1,13] the deviation of 2.7 GPa observed here is again significant. Similar to the discussion on elasticity, this deviation highlights the necessity for an all-inclusive model for the quantification of strength.[1,13] Strength levels of most Si NWs deviate from the theoretical strength of single-crystal Si estimated as 21−23 GPa.[13] In addition to the modeling and interpretation of test data, statistical analysis is also necessary due to the brittle nature of fracture.[13,93,94] Hence, as long as an appropriate model is used, increasing the number of tests will further enhance the understanding in this field.[95]

The literature can be further investigated from a modeling standpoint. For example, considering studies that rely on linear modeling, one would expect no scale effect as already demonstrated in refs 92 and 96. On the contrary, an increasing trend for modulus of elasticity with increasing critical dimensions is often reported in refs 91 and 97−99. The only investigation displaying a reduction in E with the increase of critical dimension, as presented in Figure 6, also relied on linear modeling.[100] Thus, incorporating nonlinearity into the modeling of elasticity in Si NWs appears to be highly essential. To further enhance the accuracy of interpretation, modeling efforts should take into account the influence of surface states, such as roughness, as well as the possibility of defects formation during NW fabrication.[94,96,101,102]

By performing a benchmark analysis of the $F-w$ response of a single Si NW using various models, this paper addresses the origins of the scatter of basic Si NW properties in the literature. It is supported by a careful analysis of intrinsic stresses as well as the anisotropic modeling of all NW surfaces with the actual oxide layer. Possibility of compressive intrinsic stresses in previous bottom-up Si NW studies makes it exceedingly challenging to compare recent findings with those in earlier literature. However, the benchmark study presented in this work should encourage a cautious approach to the prediction of nanomechanical properties. Despite being more complex, the need for a reliable model is justified by the current fragmented state of the literature on both the elastic and strength properties of Si NWs. Considering all relevant terms that affect the mechanical behavior, the ExtZP model represents a superior approach to the interpretation of test data with minimal assumptions. Simplifications such as avoiding intrinsic and surface effects have to be avoided. In addition to selecting a model, there are other requirements for refining E and S estimations for Si NWs. Increasing the number of tests, along with rigorous statistical treatments, is one of them. Finally, extra caution should be exercised when comparing experimental results obtained on nanostructures to computational findings on pristine crystals.

CONCLUSION

As bending tests are the leading type of nanomechanical characterization technique applied to all types of one-dimensional nanoscale building blocks including Si NWs, their interpretation through appropriate modeling is of utmost importance. In this regard, the ExtZP model introduces two critical parameters into the treatment of the bending response of Si NWs. First, intrinsic stresses are considered, which are composed of initial residual stresses and surface-induced residual stresses and are obtained through Raman spectrosco-

https://doi.org/10.1021/acsanm.3c02077
ACS Appl. Nano Mater. 2023, 6, 15465−15478

py. Similarly, surface stress and elasticity components are obtained in an anisotropic fashion, thus taking the crystalline orientation and native oxide presence on all Si NW surfaces into account. Results on pristine Si surfaces are used for validation purposes and are then compared to those obtained on oxidized surfaces. Significant variations in surface mechanical properties are induced by oxidation. The inclusion of oxide is found to magnify anisotropic effects, resulting in increased orientation dependence in properties such as f_{22} and d_{22}, which may account for previous experimental observations. By demonstrating stress fluctuations ranging from −3 to +3 N/m in unreconstructed Si films and from −12 to +12 N/m in $aSiO_2$−Si films, the observed results offer a greater comprehension of the stiffening or softening effects that result from the formation of native oxide.

On the experimental side, *in situ* bending test data are obtained on a single Si NW with its intrinsic stress state quantified by Raman spectroscopy. The resulting load−deflection curve is then interpreted through a series of models with increasing complexity, including the ExtZP model as the most involved one. Findings demonstrate a spread of 85 GPa for the modulus of elasticity. The results acquired from the models are also compared and contrasted with the previous literature that focused on the modulus of elasticity of ⟨110⟩-oriented Si NWs. Considering the fact that Si NWs are one of the most studied and most commonly employed nanoscale building blocks, it would be reasonable to assume that other materials suffer from the same extent of oversimplification in the interpretation of bending test results. A similar conclusion is reached for strength with variations of up to 3 GPa among the aforementioned nanomechanical models. It is to be emphasized that as a single test data was analyzed through different models resulting in this significant level of variation, this approach does not exclude the statistical nature of fracture. It can similarly be improved by incorporating other surface parameters such as roughness. Precise consideration of the NW surface state is thus critical to comprehend the mechanical behavior of Si NWs accurately. Although parameters such as anisotropic treatment of NW surfaces including crystal orientation of side surfaces and the presence of native oxide have so far been excluded from the nanomechanical models, this work shows their consideration makes a significant difference. It thus highlights the need for a multiscale theoretical framework to fully understand the size-dependent mechanical behavior of Si NWs and other one-dimensional nanostructures. This understanding will be crucial for the improvement of design and reliability assessment, and therefore the commercialization, of future nanoelectromechanical systems.

■ ASSOCIATED CONTENT

Supporting Information

The Supporting Information is available free of charge at https://pubs.acs.org/doi/10.1021/acsanm.3c02077.

Fit curves obtained from Heidelberg,[23] Hudson,[28] Zhan,[29] and SimpZP[21] models given in Figure S1; surface properties including surface stress components (f_{11} and f_{22}) and surface elastic constants (d_{11} and d_{22}) given in Table 2 are presented graphically in Figure S2 (PDF)

■ AUTHOR INFORMATION

Corresponding Author

B. Erdem Alaca − *Department of Mechanical Engineering, Koç University, Istanbul 34450, Turkey; n²STAR-Koç University Nanofabrication and Nanocharacterization Center for Scientific and Technological Advanced Research and Koç University Surface Technologies Research Center (KUYTAM), Koç University, Istanbul 34450, Turkey;* orcid.org/0000-0001-5931-8134; Email: ealaca@ku.edu.tr

Authors

Sina Zare Pakzad − *Department of Mechanical Engineering, Koç University, Istanbul 34450, Turkey;* orcid.org/0000-0002-7029-4812

Mohammad Nasr Esfahani − *School of Physics, Engineering and Technology, University of York, York YO10 5DD, U.K.;* orcid.org/0000-0002-6973-2205

Zuhal Tasdemir − *Laboratory of Micro and Nanotechnology, Paul Scherrer Institute, Villigen CH-5232, Switzerland*

Nicole Wollschläger − *Department 5.1: Materialography, fractography and aging of technical materials, Bundesanstalt für Materialforschung und -prüfung (BAM), Berlin 12205, Germany*

Taotao Li − *School of Electronic Science and Engineering, Nanjing University, Jiangsu 210093, China;* orcid.org/0000-0002-2815-3856

XueFei Li − *School of Electronic Science and Engineering, Nanjing University, Jiangsu 210093, China*

Mustafa Yilmaz − *Department of Mechanical Engineering, Koç University, Istanbul 34450, Turkey*

Yusuf Leblebici − *Microelectronic Systems Laboratory, Swiss Federal Institute of Technology − Lausanne (EPFL), Lausanne CH-1015, Switzerland; Rectorate, Sabanci University, Istanbul 34956, Turkey*

Complete contact information is available at: https://pubs.acs.org/10.1021/acsanm.3c02077

Notes

The authors declare no competing financial interest.

■ ACKNOWLEDGMENTS

S.Z.P. and B.E.A. gratefully acknowledge financial support by Tubitak under Grant 120E347.

■ REFERENCES

(1) Nasr Esfahani, M.; Alaca, B. E. A Review on Size-Dependent Mechanical Properties of Nanowires. *Adv. Eng. Mater.* **2019**, *21*, 1900192.

(2) Arjmand, T.; Legallais, M.; Nguyen, T. T. T.; Serre, P.; Vallejo-Perez, M.; Morisot, F.; Salem, B.; Ternon, C. Functional devices from bottom-up Silicon nanowires: A review. *Nanomaterials* **2022**, *12*, 1043.

(3) Iakab, S. A.; Rafols, P.; García-Altares, M.; Yanes, O.; Correig, X. Silicon-based laser desorption ionization mass spectrometry for the analysis of biomolecules: a progress report. *Adv. Funct. Mater.* **2019**, *29*, 1903609.

(4) Sage, E.; Sansa, M.; Fostner, S.; Defoort, M.; Gély, M.; Naik, A. K.; Morel, R.; Duraffourg, L.; Roukes, M. L.; Alava, T.; Jourdan, G.; Colinet, E.; Masselon, C.; Brenac, A.; Hentz, S. Single-particle mass spectrometry with arrays of frequency-addressed nanomechanical resonators. *Nat. Commun.* **2018**, *9*, 1−8.

(5) Alaca, B. E.; Karimzadehkhouei, M. Piezoresistive nanowire-based electromechanical sensors. Elsevier, 2023.

(6) Zhang, G.-J.; Zhang, L.; Huang, M. J.; Luo, Z. H. H.; Tay, G. K. I.; Lim, E.-J. A.; Kang, T. G.; Chen, Y. Silicon nanowire biosensor for highly sensitive and rapid detection of Dengue virus. *Sens. Actuators, B* **2010**, *146*, 138−144.
(7) Zafar, S.; D'Emic, C.; Jagtiani, A.; Kratschmer, E.; Miao, X.; Zhu, Y.; Mo, R.; Sosa, N.; Hamann, H.; Shahidi, G.; Riel, H. Silicon nanowire field effect transistor sensors with minimal sensor-to-sensor variations and enhanced sensing characteristics. *ACS Nano* **2018**, *12*, 6577−6587.
(8) Sessi, V.; Simon, M.; Mulaosmanovic, H.; Pohl, D.; Loeffler, M.; Mauersberger, T.; Fengler, F. P.; Mittmann, T.; Richter, C.; Slesazeck, S.; Mikolajick, T.; Weber, W. M. A Silicon Nanowire Ferroelectric Field-Effect Transistor. *Adv. Electron. Mater.* **2020**, *6*, 1901244.
(9) Li, X.; Yang, X.; Zhang, Z.; Wang, T.; Sun, Y.; Liu, Z.; Li, X.; Shi, Y.; Xu, J. Impact of process fluctuations on reconfigurable silicon nanowire transistor. *IEEE Trans. Electron Devices* **2021**, *68*, 885−891.
(10) Nehra, M.; Dilbaghi, N.; Marrazza, G.; Kaushik, A.; Abolhassani, R.; Mishra, Y. K.; Kim, K. H.; Kumar, S. 1D semiconductor nanowires for energy conversion, harvesting and storage applications. *Nano Energy* **2020**, *76*, 104991.
(11) Cakirlar, C.; Galderisi, G.; Beyer, C.; Simon, M.; Mikolajick, T.; Trommer, J. *Challenges in Electron Beam Lithography of Silicon Nanostructures*. 2022 IEEE 22nd International Conference on Nanotechnology (NANO), 2022; pp 207−210.
(12) Yang, C.; Van Der Drift, E.; French, P. Review of scaling effects on physical properties and practicalities of cantilever sensors. *J. Micromech. Microeng.* **2022**, *32*, 103002.
(13) DelRio, F. W.; Cook, R. F.; Boyce, B. L. Fracture strength of micro-and nano-scale silicon components. *Appl. Phys. Rev.* **2015**, *2*, 021303.
(14) Stassi, S.; Cooperstein, I.; Tortello, M.; Pirri, C. F.; Magdassi, S.; Ricciardi, C. Reaching silicon-based NEMS performances with 3D printed nanomechanical resonators. *Nat. Commun.* **2021**, *12*, 1−9.
(15) Yang, J.; Ono, T.; Esashi, M. Energy dissipation in submicrometer thick single-crystal silicon cantilevers. *J. Microelectromech. Syst.* **2002**, *11*, 775−783.
(16) Cui, Y.; Zhong, Z.; Wang, D.; Wang, W. U.; Lieber, C. M. High performance silicon nanowire field effect transistors. *Nano Lett.* **2003**, *3*, 149−152.
(17) Espinosa, H. D.; Bernal, R. A.; Filleter, T. In-Situ TEM Electromechanical Testing of Nanowires and Nanotubes. *Nano and Cell Mechanics: Fundamentals and Frontiers* **2012**, 191−226.
(18) Wang, S.; Shan, Z.; Huang, H. The mechanical properties of nanowires. *Advanced Science* **2017**, *4*, 1600332.
(19) Pakzad, S. Z.; Esfahani, M. N.; Alaca, B. E. The role of native oxide on the mechanical behavior of silicon nanowires. *Mater. Today Commun.* **2023**, *34*, 105002.
(20) Pakzad, S. Z.; Esfahani, M. N.; Alaca, B. E. Molecular Dynamics Study of Orientation-dependent Tensile Properties of Si Nanowires with Native Oxide: Surface Stress and Surface Energy Effects. *2021 IEEE 21st International Conference on Nanotechnology (NANO)*, 2021; pp 370−373.
(21) Zare Pakzad, S.; Nasr Esfahani, M.; Tasdemir, Z.; Wollschlaeger, N.; Li, X.; Li, T.; Yilmaz, M.; Leblebici, Y.; Alaca, B. E. A new characterization approach to study the mechanical behavior of silicon nanowires. *Mrs Advances* **2021**, *6*, 500−505.
(22) Tasdemir, Z.; Peric, O.; Sacchetto, D.; Fantner, G. E.; Leblebici, Y.; Alaca, B. E. Monolithic fabrication of silicon nanowires bridging thick silicon structures. *IEEE Transactions on Nanotechnology* **2018**, *17*, 1299−1302.
(23) Heidelberg, A.; Ngo, L. T.; Wu, B.; Phillips, M. A.; Sharma, S.; Kamins, T. I.; Sader, J. E.; Boland, J. J. A generalized description of the elastic properties of nanowires. *Nano Lett.* **2006**, *6*, 1101−1106.
(24) Elhebeary, M.; Saif, M. T. A. A novel mems stage for in-situ thermomechanical testing of single crystal silicon microbeams under bending. *Extreme Mechanics Letters* **2018**, *23*, 1−8.
(25) Wollschläger, N.; Tasdemir, Z.; Häusler, I.; Leblebici, Y.; Österle, W.; Alaca, B. E. Determination of the elastic behavior of silicon nanowires within a scanning electron microscope. *J. Nanomater.* **2016**, *2016*, 36.
(26) Brand, U.; Xu, M.; Doering, L.; Langfahl-Klabes, J.; Behle, H.; Bütefisch, S.; Ahbe, T.; Peiner, E.; Völlmeke, S.; Frank, T.; Mickan, B.; Kiselev, I.; Hauptmannl, M.; Drexel, M. Long slender piezoresistive silicon microprobes for fast measurements of roughness and mechanical properties inside micro-holes with diameters below 100 μm. *Sensors* **2019**, *19*, 1410.
(27) Ngo, L. T.; Almécija, D.; Sader, J. E.; Daly, B.; Petkov, N.; Holmes, J. D.; Erts, D.; Boland, J. J. Ultimate-strength germanium nanowires. *Nano Lett.* **2006**, *6*, 2964−2968.
(28) Hudson, S. D.; Zhurov, V.; Grbić, V.; Grbić, M.; Hutter, J. L. Measurement of the elastic modulus of spider mite silk fibers using atomic force microscopy. *J. Appl. Phys.* **2013**, *113*, 154307.
(29) Zhan, H.; Gu, Y. Modified beam theories for bending properties of nanowires considering surface/intrinsic effects and axial extension effect. *J. Appl. Phys.* **2012**, *111*, 084305.
(30) Yaish, Y.; Calahorra, Y.; Shtempluck, O.; Kotchetkov, V. Three-point bending analysis of doubly clamped silicon nanowire beams; Young's modulus, initial stress, and crystal orientation. *J. Appl. Phys.* **2015**, *117*, 164311.
(31) Calahorra, Y.; Shtempluck, O.; Kotchetkov, V.; Yaish, Y. Young's modulus, residual stress, and crystal orientation of doubly clamped silicon nanowire beams. *Nano Lett.* **2015**, *15*, 2945−2950.
(32) He, J.; Lilley, C. M. Surface effect on the elastic behavior of static bending nanowires. *Nano Lett.* **2008**, *8*, 1798−1802.
(33) Song, F.; Huang, G.; Park, H.; Liu, X. A continuum model for the mechanical behavior of nanowires including surface and surface-induced initial stresses. *International Journal of Solids and Structures* **2011**, *48*, 2154−2163.
(34) Nasr Esfahani, M.; Zare Pakzad, S.; Li, T.; Li, X.; Tasdemir, Z.; Wollschläger, N.; Leblebici, Y.; Alaca, B. E. Effect of Native Oxide on Stress in Silicon Nanowires: Implications for Nanoelectromechanical Systems. *ACS Appl. Nano Mater.* **2022**, *5*, 13276−13285.
(35) Zare Pakzad, S.; Nasr Esfahani, M.; Alaca, B. E. Mechanical Properties of Silicon Nanowires with Native Oxide Surface State. *arXiv preprint arXiv:2307.03650*, 2023.
(36) Agrawal, R.; Peng, B.; Gdoutos, E. E.; Espinosa, H. D. Elasticity size effects in ZnO nanowires- a combined experimental-computational approach. *Nano Lett.* **2008**, *8*, 3668−3674.
(37) McDowell, M. T.; Lee, S. W.; Ryu, I.; Wu, H.; Nix, W. D.; Choi, J. W.; Cui, Y. Novel size and surface oxide effects in silicon nanowires as lithium battery anodes. *Nano Lett.* **2011**, *11*, 4018−4025.
(38) Ohta, H.; Watanabe, T.; Ohdomari, I. Strain distribution around SiO_2/Si interface in Si nanowires: a molecular dynamics study. *Japanese journal of applied physics* **2007**, *46*, 3277.
(39) Izumi, S.; Hara, S.; Kumagai, T.; Sakai, S. A method for calculating surface stress and surface elastic constants by molecular dynamics: application to the surface of crystal and amorphous silicon. *Thin Solid Films* **2004**, *467*, 253−260.
(40) Gurtin, M. E.; Ian Murdoch, A. A continuum theory of elastic material surfaces. *Archive for rational mechanics and analysis* **1975**, *57*, 291−323.
(41) Steigmann, D.; Ogden, R. Plane deformations of elastic solids with intrinsic boundary elasticity. *Proc. R. Soc. London. Series A: Mathematical, Physical and Engineering Sciences* **1997**, *453*, 853−877.
(42) Chhapadia, P.; Mohammadi, P.; Sharma, P. Curvature-dependent surface energy and implications for nanostructures. *J. Mech. Phys. Solids* **2011**, *59*, 2103−2115.
(43) Chiu, M.-S.; Chen, T. Effects of high-order surface stress on static bending behavior of nanowires. *Physica E: Low-dimensional Systems and Nanostructures* **2011**, *44*, 714−718.
(44) Chen, T.; Chiu, M.-S.; Weng, C.-N. Derivation of the generalized Young-Laplace equation of curved interfaces in nano-scaled solids. *J. Appl. Phys.* **2006**, *100*, 074308.
(45) Zhang, Y.; Cai, J.; Mi, C.; Wang, F.; Akbarzadeh, A. Effect of surface residual stress and surface layer stiffness on mechanical properties of nanowires. *Acta Mechanica* **2022**, *233*, 233−257.

https://doi.org/10.1021/acsanm.3c02077
ACS Appl. Nano Mater. 2023, 6, 15465−15478

(46) Song, F.; Huang, G. Modeling of surface stress effects on bending behavior of nanowires: Incremental deformation theory. *Phys. Lett. A* **2009**, *373*, 3969−3973.
(47) Dolabella, S.; Frison, R.; Chahine, G. A.; Richter, C.; Schulli, T. U.; Tasdemir, Z.; Alaca, B. E.; Leblebici, Y.; Dommann, A.; Neels, A. Real-and Q-space travelling: multi-dimensional distribution maps of crystal-lattice strain ($\epsilon_0$44) and tilt of suspended monolithic silicon nanowire structures. *Journal of applied crystallography* **2020**, *53*, 58−68.
(48) Wang, G.-F.; Feng, X.-Q. Effects of surface elasticity and residual surface tension on the natural frequency of microbeams. *Appl. Phys. Lett.* **2007**, *90*, 231904.
(49) Li, X.-F.; Zhang, H.; Lee, K. Y. Dependence of Young's modulus of nanowires on surface effect. *International Journal of Mechanical Sciences* **2014**, *81*, 120−125.
(50) Xiao, Y.; Shang, J.; Kou, L.; Li, C. Surface deformation-dependent mechanical properties of bending nanowires: an ab initio core-shell model. *Applied Mathematics and Mechanics* **2022**, *43*, 219−232.
(51) Massa, E.; Sasso, C. P.; Mana, G. The measurement of the silicon lattice parameter and the count of atoms to realise the kilogram. *MAPAN* **2020**, *35*, 511−519.
(52) Pennelli, G.; Totaro, M.; Nannini, A. Correlation between surface stress and apparent Young's modulus of top-down silicon nanowires. *ACS Nano* **2012**, *6*, 10727−10734.
(53) Melis, C.; Giordano, S.; Colombo, L.; Mana, G. Density functional theory calculations of the stress of oxidised (1 1 0) silicon surfaces. *Metrologia* **2016**, *53*, 1339.
(54) Miller, R. E.; Shenoy, V. B. Size-dependent elastic properties of nanosized structural elements. *Nanotechnology* **2000**, *11*, 139.
(55) Diao, J.; Gall, K.; Dunn, M. L. Atomistic simulation of the structure and elastic properties of gold nanowires. *J. Mech. Phys. Solids* **2004**, *52*, 1935−1962.
(56) Lee, B.; Rudd, R. E. First-principles study of the Young's modulus of Si< 001> nanowires. *Phys. Rev. B* **2007**, *75*, 041305.
(57) Li, J.; Lei, X.; Ding, J.; Gao, Z.; Wang, H.; Shi, Y. Surface effect on size dependent Young's modulus of nanowires: Exponentially decreased surface elasticity model. *Mater. Lett.* **2022**, *307*, 131001.
(58) Yao, H.; Yun, G.; Bai, N.; Li, J. Surface elasticity effect on the size-dependent elastic property of nanowires. *J. Appl. Phys.* **2012**, *111*, 083506.
(59) Xu, X.-J.; Wang, Y.-C.; Wang, B.; Zhang, K. A modified size-dependent core−shell model and its application in the wave propagation of square cellular networks. *Physica E: Low-dimensional Systems and Nanostructures* **2016**, *80*, 53−61.
(60) Stan, G.; Ciobanu, C.; Parthangal, P. M.; Cook, R. F. Diameter-dependent radial and tangential elastic moduli of ZnO nanowires. *Nano Lett.* **2007**, *7*, 3691−3697.
(61) Bauchau, O. A.; Craig, J. I. Euler-Bernoulli beam theory. *Structural analysis* **2009**, *163*, 173−221.
(62) Mills, S.; Sader, J. E.; Boland, J. J. Material characterisation of nanowires with intrinsic stress. *Nanotechnology* **2017**, *28*, 355706.
(63) Plimpton, S. Fast parallel algorithms for short-range molecular dynamics. *J. Comput. Phys.* **1995**, *117*, 1−19.
(64) Van Duin, A. C.; Strachan, A.; Stewman, S.; Zhang, Q.; Xu, X.; Goddard, W. A. ReaxFFSiO reactive force field for silicon and silicon oxide systems. *J. Phys. Chem. A* **2003**, *107*, 3803−3811.
(65) Khalilov, U.; Pourtois, G.; Bogaerts, A.; Van Duin, A. C.; Neyts, E. C. Reactive molecular dynamics simulations on SiO 2-coated ultra-small Si-nanowires. *Nanoscale* **2013**, *5*, 719−725.
(66) Khalilov, U.; Pourtois, G.; Huygh, S.; Van Duin, A.; Neyts, E.; Bogaerts, A. New mechanism for oxidation of native silicon oxide. *J. Phys. Chem. C* **2013**, *117*, 9819−9825.
(67) Newsome, D. A.; Sengupta, D.; Foroutan, H.; Russo, M. F.; Van Duin, A. C. Oxidation of silicon carbide by O2 and H_2O: a ReaxFF reactive molecular dynamics study, Part I. *J. Phys. Chem. C* **2012**, *116*, 16111−16121.
(68) Pishkenari, H. N.; Rezaei, S. Characterization of silicon surface elastic constants based on different interatomic potentials. *Thin Solid Films* **2017**, *626*, 104−109.
(69) Xu, W.; Kim, W. K. Molecular dynamics simulation of the uniaxial tensile test of silicon nanowires using the MEAM potential. *Mech. Mater.* **2019**, *137*, 103140.
(70) Park, H. S. Surface stress effects on the resonant properties of silicon nanowires. *J. Appl. Phys.* **2008**, *103*, 123504.
(71) Melis, C.; Colombo, L.; Mana, G. Lattice strain at c-Si surfaces: a density functional theory calculation. *Metrologia* **2015**, *52*, 214.
(72) Jung, H.-E.; Shin, M. Effects of Si/SiO_2 interface stress on the performance of ultra-thin-body field effect transistors: a first-principles study. *Nanotechnology* **2018**, *29*, 025201.
(73) Quagliotti, D.; Mana, G.; Massa, E.; Sasso, C.; Kuetgens, U. A finite element analysis of surface-stress effects on measurement of the Si lattice parameter. *Metrologia* **2013**, *50*, 243.
(74) Delph, T. Near-surface stresses in silicon (0 0 1). *Surface science* **2008**, *602*, 259−267.
(75) Payne, M.; Roberts, N.; Needs, R.; Needels, M.; Joannopoulos, J. Total energy and stress of metal and semiconductor surfaces. *Surf. Sci.* **1989**, *211*, 1−20.
(76) Miyamoto, Y. Comparative study of Si (100) surface stresses with dimerized group-IV adatoms. *Phys. Rev. B* **1994**, *49*, 1947.
(77) Alerhand, O.; Vanderbilt, D.; Meade, R. D.; Joannopoulos, J. Spontaneous formation of stress domains on crystal surfaces. *Physical review letters* **1988**, *61*, 1973.
(78) Munetoh, S.; Motooka, T.; Moriguchi, K.; Shintani, A. Interatomic potential for Si−O systems using Tersoff parameterization. *Comput. Mater. Sci.* **2007**, *39*, 334−339.
(79) Zimmerman, J. A.; WebbIII, E. B.; Hoyt, J.; Jones, R. E.; Klein, P.; Bammann, D. J. Calculation of stress in atomistic simulation. *Modell. Simul. Mater. Sci. Eng.* **2004**, *12*, S319.
(80) Tasdemir, Z.; Wollschläger, N.; Österle, W.; Leblebici, Y.; Alaca, B. E. A deep etching mechanism for trench-bridging silicon nanowires. *Nanotechnology* **2016**, *27*, 095303.
(81) Esfahani, M. N.; Kilinc, Y.; Karakan, M. Ç.; Orhan, E.; Hanay, M. S.; Leblebici, Y.; Alaca, B. E. Piezoresistive silicon nanowire resonators as embedded building blocks in thick SOI. *J. Micromech. Microeng.* **2018**, *28*, 045006.
(82) Spejo, L.; Arrieta-Concha, J.; Puydinger dos Santos, M.; Barros, A.; Bourdelle, K.; Diniz, J.; Minamisawa, R. Non-linear Raman shift-stress behavior in top-down fabricated highly strained silicon nanowires. *J. Appl. Phys.* **2020**, *128*, 045704.
(83) Hung, P.; Hong, N. Simulation study of polymorphism and diffusion anomaly for SiO_2 and GeO2 liquid. *European Physical Journal B* **2009**, *71*, 105−110.
(84) Meade, C.; Hemley, R. J.; Mao, H. High-pressure X-ray diffraction of SiO 2 glass. *Phys. Rev. Lett.* **1992**, *69*, 1387.
(85) Maras, E.; Trushin, O.; Stukowski, A.; Ala-Nissila, T.; Jonsson, H. Global transition path search for dislocation formation in Ge on Si (001). *Comput. Phys. Commun.* **2016**, *205*, 13−21.
(86) Ma, D.; Lee, C.; Au, F.; Tong, S.; Lee, S. Small-diameter silicon nanowire surfaces. *Science* **2003**, *299*, 1874−1877.
(87) Shchipalov, Y. K. Surface energy of crystalline and vitreous silica. *Glass and ceramics* **2000**, *57*, 374−377.
(88) Deal, B. E.; Grove, A. General relationship for the thermal oxidation of silicon. *Journal of applied physics* **1965**, *36*, 3770−3778.
(89) Morita, M.; Ohmi, T.; Hasegawa, E.; Kawakami, M.; Ohwada, M. Growth of native oxide on a silicon surface. *J. Appl. Phys.* **1990**, *68*, 1272−1281.
(90) Sander, D.; Ibach, H. Experimental determination of adsorbate-induced surface stress: Oxygen on Si (111) and Si (100). *Phys. Rev. B* **1991**, *43*, 4263.
(91) Han, X.; Zheng, K.; Zhang, Y.; Zhang, X.; Zhang, Z.; Wang, Z. L. Low-temperature in situ large-strain plasticity of silicon nanowires. *Adv. Mater.* **2007**, *19*, 2112−2118.
(92) Hsin, C.-L.; Mai, W.; Gu, Y.; Gao, Y.; Huang, C.-T.; Liu, Y.; Chen, L.-J.; Wang, Z.-L. Elastic properties and buckling of silicon nanowires. *Adv. Mater.* **2008**, *20*, 3919−3923.

https://doi.org/10.1021/acsanm.3c02077
ACS Appl. Nano Mater. 2023, 6, 15465−15478

(93) Cheng, G.; Zhang, Y.; Chang, T.-H.; Liu, Q.; Chen, L.; Lu, W. D.; Zhu, T.; Zhu, Y. In situ nano-thermomechanical experiment reveals brittle to ductile transition in silicon nanowires. *Nano Lett.* **2019**, *19*, 5327−5334.
(94) Tang, D.-M.; Ren, C.-L.; Wang, M.-S.; Wei, X.; Kawamoto, N.; Liu, C.; Bando, Y.; Mitome, M.; Fukata, N.; Golberg, D. Mechanical properties of Si nanowires as revealed by in situ transmission electron microscopy and molecular dynamics simulations. *Nano Lett.* **2012**, *12*, 1898−1904.
(95) Namazu, T.; Isono, Y.; Tanaka, T. Evaluation of size effect on mechanical properties of single crystal silicon by nanoscale bending test using AFM. *J. Microelectromech. Syst.* **2000**, *9*, 450−459.
(96) Zhang, H.; Tersoff, J.; Xu, S.; Chen, H.; Zhang, Q.; Zhang, K.; Yang, Y.; Lee, C.-S.; Tu, K.-N.; Li, J.; Lu, Y. Approaching the ideal elastic strain limit in silicon nanowires. *Sci. Adv.* **2016**, *2*, No. e1501382.
(97) Sadeghian, H.; Yang, C.; Goosen, J.; Van Der Drift, E.; Bossche, A.; French, P.; Van Keulen, F. Characterizing size-dependent effective elastic modulus of silicon nanocantilevers using electrostatic pull-in instability. *Appl. Phys. Lett.* **2009**, *94*, 221903.
(98) Li, X.; Ono, T.; Wang, Y.; Esashi, M. Ultrathin single-crystalline-silicon cantilever resonators: Fabrication technology and significant specimen size effect on Young's modulus. *Appl. Phys. Lett.* **2003**, *83*, 3081−3083.
(99) Zhu, Y.; Xu, F.; Qin, Q.; Fung, W. Y.; Lu, W. Mechanical properties of vapor- liquid- solid synthesized silicon nanowires. *Nano Lett.* **2009**, *9*, 3934−3939.
(100) Tsuchiya, T.; Hemmi, T.; Suzuki, J.-y.; Hirai, Y.; Tabata, O. Tensile strength of silicon nanowires batch-fabricated into electrostatic MEMS testing device. *Applied Sciences* **2018**, *8*, 880.
(101) Kim, Y.-J.; Son, K.; Choi, I.-C.; Choi, I.-S.; Park, W. I.; Jang, J.-i. Exploring nanomechanical behavior of silicon nanowires: AFM bending versus nanoindentation. *Adv. Funct. Mater.* **2011**, *21*, 279−286.
(102) Gordon, M. J.; Baron, T.; Dhalluin, F.; Gentile, P.; Ferret, P. Size effects in mechanical deformation and fracture of cantilevered silicon nanowires. *Nano Lett.* **2009**, *9*, 525−529.

https://doi.org/10.1021/acsanm.3c02077
ACS Appl. Nano Mater. 2023, 6, 15465−15478